Pergamon

Int. J. Solids Structures Vol. 35, No. 36, pp. 5139–5158, 1998

Printed in Great Britain
0020–7683/98/$—see front matter

PII: S0020–7683(97)00247–3

LINE-SPRING FINITE ELEMENT FOR FULLY PLASTIC CRACK GROWTH—II. SURFACE-CRACKED PLATES AND PIPES

HYUNGYIL LEE*
Department of Mechanical Engineering, Sogang University, Seoul, Korea

and

DAVID M. PARKS
Department of Mechanical Engineering, Massachusetts Institute of Technology, Cambridge, Massachusetts 02139, U.S.A

(*Received* 23 *November* 1996; *in revised form* 3 *August* 1997)

Abstract—Crack-tip opening angle (CTOA) is generally considered as the most operable fracture descriptor for fully plastic, quasi-steady, extensive crack extension. In Part I, based on the CTOA crack growth criterion, a line-spring finite element model was presented to resolve through-thickness crack growth in plane strain single-edge-cracked specimens and surface-cracked plate/shell structures under fully plastic loading. With constraint-dependent CTOA and some supplemental kinematic relations given, the line-spring model ultimately monitors crack extension from the history of generalized displacements. The model was implemented in the implicit ABAQUS finite element code (1993b) in a user-defined element form. Following the plane strain parametric studies in Part I, we further apply the line-spring model to the problems of surface-cracked plates and pipes in Part II here. Effects of material hardening, configuration and location of the surface crack on the histories of penetration-displacement/pressure are examined in a remotely-stretched plate and a pressurized cylindrical vessel. As the most plausible exercise of a stable crack propagation leading to leak-before-break failure, a circumferentially cracked pipe subject to pure bending is selected. Evolution of CTOA along the crack-front and surface crack enlargement pattern are examined for each case. Experimentally-observed CTOA values for the remotely-stretched plate are interpreted in light of the model prediction.

1. INTRODUCTION

In the safety assessment of pressure vessels and pipes, primary concern is often given to the occurrence of the failure mode known as leak-before-break (LBB). If the leakage of fluid via a subcritical through-crack is detected in one way or another, a remedial action such as shutdown of the system to prevent a global failure can be taken. Since a loss of contained fluid is likely to be followed by an internal pressure drop, LBB can in some sense be viewed as a possible outcome of a 'desirable' (at least, 'preferable') sequence of events—penetration of a crack through-thickness, but no immediate unstable crack propagation along the wall (Kanninen and Popelar, 1985). By providing guidelines for design and material selection, an established LBB methodology could bring about enormous cost savings in manufacturing and maintenance of the pressurized vessel and piping systems.

With ultimate applications to LBB analyses in mind, Lee and Parks (1998), hereafter referred to as Part I, developed an advanced line-spring model for fully plastic quasi-steady crack growth of plane strain single-edge-cracked (SEC) specimens, and surface-cracked shell structures. Ductile crack growth results from the nucleation, growth and coalescence of microscopic voids. Evolution of voids is in turn influenced by the near-field plasticity. Correlating micromechanisms and near-field plastic parameters, CTOA is thought of as the most operable fracture descriptor of such strain-controlled fracture process. In the line-spring model, the CTOA is evaluated using the sliding-off and cracking model of McClintock *et al.* (1995) together with the least upper bound method of Kim *et al.* (1996). CTOA

* Author to whom all correspondence should be addressed.

in the sliding-off and cracking model is viewed as a material-dependent function of stress and strain imposed on the moving crack-tip. Upon determining the constraint-dependent CTOA, the increment of crack extension is kinematically determined from the loading-imposed increment of crack-tip opening displacement (CTOD). Details of the crack-growth line-spring constitutive relations are given in Part I. The model was incorporated into the implicit ABAQUS finite element code (1993b) in the form of a user-defined element.

Parametric studies in Part I on plane strain SEC specimens revealed that the loading type and material hardening are responsible for the load increase after crack initiation and crack propagation rate per unit imposed displacement. It was also shown that delayed crack initiation, longer specimen length, higher yield strength, lower ductility and initially shorter crack, each inclines the SEC specimen to unstable cracking. The line-spring system characteristics derived for a plane strain SEC specimen under remote pure tension readily accounted for how those parameters influence the system stability. Here in Part II, we apply the line-spring model to problems of surface-cracked plates and pipes.

We first model a surface-cracked plate under remote tension. Effects of material hardening and crack configuration on the surface crack propagation are examined. Experimentally observed CTOA values are interpreted in light of the model prediction. we then consider axial surface cracks in an internally pressurized vessel. Again, effects of crack configuration and location (internal/external) on the surface crack extension and CTOA variation along the surface crack front are addressed in connection with elastic solutions. Finally, motivated by the remarkably relaxed crack-front stress field reported by Kikuchi (1992), we select a part-through circumferentially-cracked pipe subject to pure bending. This crack geometry and loading gives the most plausible exercise of stable crack propagation leading to LBB failure. Surface crack enlargement pattern, and evolution of local CTOA and crack depth are presented.

2. LINE-SPRING DEVELOPMENT

A subcritical crack under normal operating conditions typically initiates at the inner surface of the vessel and pipe wall, then grows by combined fatigue and/or stress corrosion to form a surface crack. In consequence of such process, surface cracks are often encountered in practice, and have been a primary concern in the field of engineering fracture mechanics. Due to their intrinsic three-dimensional nature, surface/corner crack problems are generally analyzed with numerical techniques. However, it is not currently feasible to solve problems of extended ductile surface crack growth by using conventional 3-D continuum finite element methods, even with state-of-the-art computer resources and FEM software. Therefore, a simple but accurate mechanics model of surface crack behavior is in great need.

For an effective evaluation of the stress intensity factor (K_I) in part-through surface-cracked plates and shells, Rice and levy (1972) devised the line-spring model. The concept was extended to elastic-plastic problems in the incremental theory of plasticity by Rice (1972) and Parks *et al.* (Parks, 1981; Parks and White, 1982; White *et al.*, 1983). The model was then further applied to the two-parameter characterization of elastic-plastic crack-tip stress fields along the surface crack front (Wang and Parks, 1992; Wang, 1993; Lee and Parks, 1995). One of the most attractive, yet unexploited, features of the line-spring model is that it can simulate an arbitrary crack growth in the thickness direction without any finite element remeshing. A crack-growth line-spring model based on the J-integral was attempted by Miyoshi *et al.* (1986) using deformation theory of plasticity. However, a J-based fracture criterion and the deformation theory of plasticity upon which it is ultimately based are limited to amounts of crack growth small in comparison to initial ligament size (Hutchinson and Paris, 1979). Therefore, to handle extensive surface crack growth, Lee and Parks (1998) presented a crack-growth line-spring model based on flow theory plasticity and a constraint-sensitive CTOA fracture criterion. In our line-spring model, CTOA in general varies both along the surface crack front at fixed load, and at fixed crack front location, with respect to the applied load.

3. RESULTS

3.1. *A remotely-stretched surface cracked plate*

Reuter and Lloyd (1990) (herein denoted 'RL') experimentally measured the CTOD and CTOA around the surface-crack perimeters during fully plastic crack growth by testing replicate specimens to varying load-crosshead displacements. Figure 1 is a schematic view of a surface-cracked plate having a length $2h$, a width $2b$ and a thickness t. The semi-elliptical crack in the center of the plate has a surface length $2c$ and a maximum through-thickness penetration a. Because the parametric angle ϕ requires an elliptical crack shape, ϕ holds its meaning only until the crack initiation. Once crack extension commences, the distance x measured from the surface-crack center line is more useful than ϕ in locating the crack front position of the growing crack. Surface-cracked plate specimens had geometric ratios $h/t = 20$, $b/t = 8$ and $a/c = 0.24$. Given the symmetry of geometry and loading, only one-quarter of a plate was modeled by eight-node shell elements with reduced integration (element type S8R from the ABAQUS library, 1993b). For an adequate elastic-plastic compliance in response to the remote bending moment, 9 Simpson's rule integration points across the thickness of the shell were used. Ten 3-node second order line-spring elements assuming a symmetry plane cross the spring represented the cracked plane.

Figure 2(a) is the normalized load vs displacement curve under remote extension, meaning $N^\infty > 0$, $\theta^\infty = 0$ in Fig. 1. We used a multi-linear stress/strain curve, smoothly approximating the experimental data for ASTM A710 Grade A steel. In A710 steel, the strain hardening exponent is near $n \doteq 10$ and $\sigma_u/\sigma_y \doteq 1.35$, where σ_u is the tensile strength occurring at about 8% strain (Reuter and Lloyd, 1990). The critical CTOD value at crack initiation for this material ranges from $\delta_i^c = 0.22$ mm to $\delta_i^c = 0.35$ mm, depending on crack-tip constraint (Hancock *et al.*, 1993). For crack initiation, we used a constant critical CTOD value of $\delta_i^c = 0.25$ mm, along the entire crack front. The relative ratio of critical CTOD to plate thickness is thus $\delta_i^c/t = 0.25/6.4 \doteq 0.039$. Because δ_i^c in general depends on the crack-tip triaxiality, it should actually vary along the crack front. However, the crack configuration tested here has a very flat border due to the low aspect ratio $a/c = 0.24$; thus the constant value of δ_i^c seems acceptable as a first order approximation. Experiments by RL in fact showed quite gradual (moderate) variation of δ_i^c along most of the crack front. The

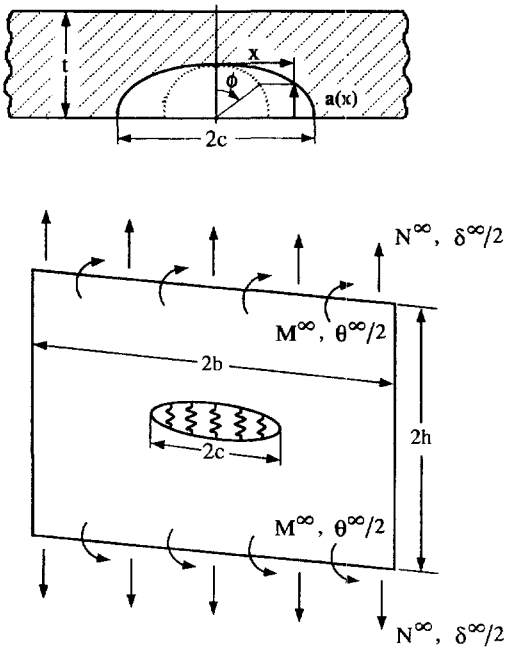

Fig. 1. Cross section of a part-through surface crack with a length $2c$ and varying depth $a(x)$ in a shell of thickness t (above). Schematic illustration of line-spring model which converts the part-through surface crack to the through-crack with a generalized foundation (below).

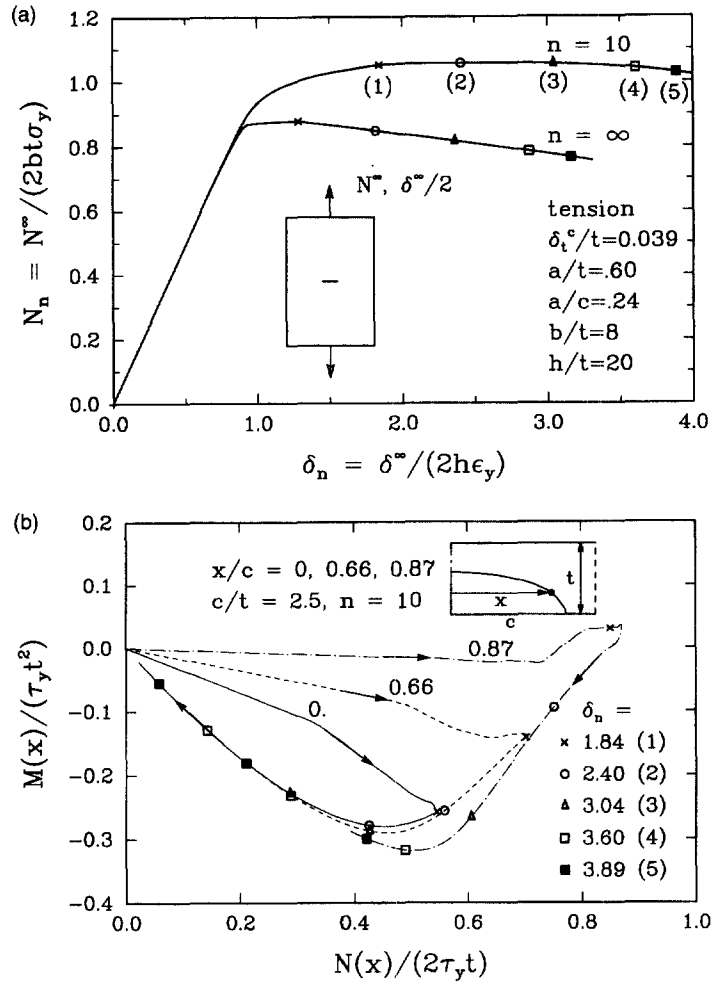

Fig. 2. (a) Normalized load N_n vs displacement δ_n curve under remote extension ($N^\infty > 0$, $\theta^\infty = 0$ in Fig. 2). The point denoted by (1) is the crack initiation point at the mid-section ($x/c = 0$). A constant critical CTOD value of $\delta_t^c = 0.25$ mm was used throughout the crack front. (b) Normalized force and bending moment trajectory transmitted across the line-spring elements at three crack front positions, $x/c = 0$, 0.66 and 0.87. (c) Normalized load N_n vs displacement δ_n curve under remote extension. Effect of initial center-line crack depth ($a(x = 0)/t = 0.6$, 0.67). (d) Normalized load N_n vs displacement δ_n curve under remote extension. Effect of material ductility ($A = 0.5$, 0.6).

material ductility parameters A and B in eqn (3) of Part I are taken as $A = 0.5$ and $B = 0$. A is related to a strain for hole growth to linkage by micro-rupture, and B to a strain for hole nucleation. Details are given in Part I. The point denoted by (1) in Fig. 2(a) is the calculated crack initiation point at the mid-section ($x/t = 0$), and point (5) corresponds to the load level where mid-section crack depth has grown to $a/t \approx 0.96$; see Fig. 4(b). After fully plastic yielding of the plate, the computed reaction force N^∞ saturates immediately, and shows small variation (3%) in its magnitude in spite of the significant net-section reduction due to surface crack growth. In the same simulation, but with non-hardening material, the reaction force N^∞ steadily decreases more than 14% from its peak value, indicated by the cross symbol '×', as the surface crack grows. Figure 2(b) shows the trajectories of normalized force and bending moment transmitted across the line-spring elements at three locations. The positions $x/c = 0.$, 0.66 and 0.87 on the original surface crack front are marked by cross symbols '×' in Fig. 4(b). Near the free surface ($x/c = 0.87$), the loading starts near pure tension ($N > 0$, $M \approx 0$), then approaches pure extension ($N > 0$, $\theta \approx 0$). Note that $N(x)$ and $M(x)$ are membrane force and bending moment per unit length transmitted by the line-spring element at x, and relative separation and rotation $[\delta(x), \theta(x)]$ are work-conjugates to $[N(x), M(x)]$; see Part I. Trajectories of resultant force

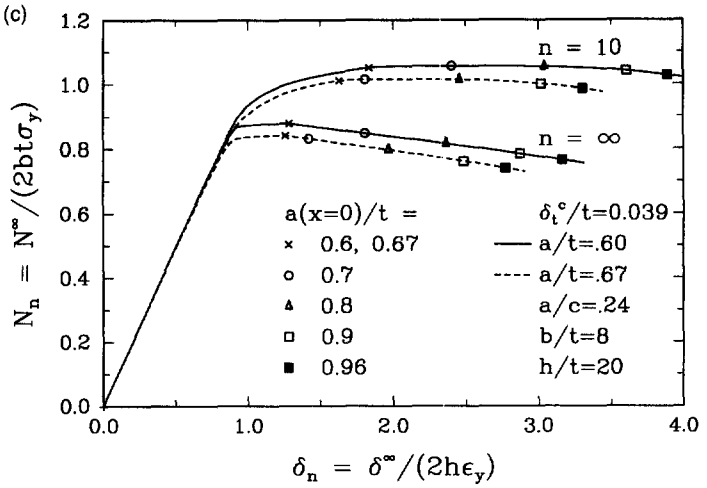

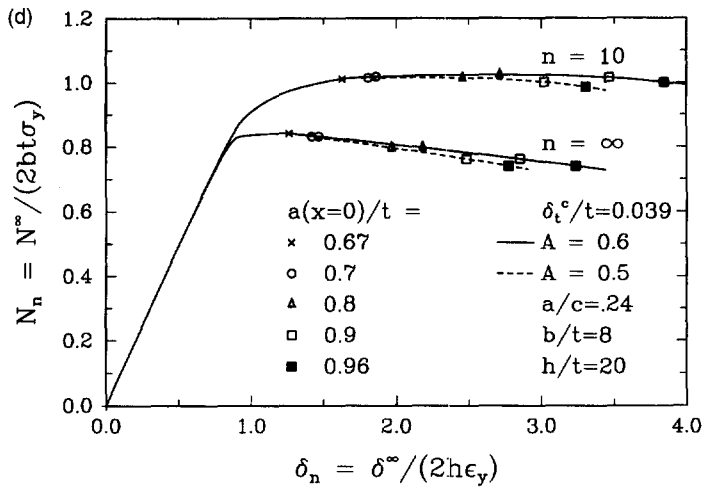

Fig. 2.—*Continued.*

and moment at three different crack front locations follow similar paths. Considering 10% variation of $a(x = 0)/t$-values in experimentally tested replicate specimens of RL, we also analyzed the other extreme case of $a/t = 0.67$. The effects of initial center-line crack depth [$a(x = 0)/t = 0.6, 0.67$], and material ductility ($A = 0.5, 0.6$) are given in Figs 2(c) and (d), respectively. An initially deeper and longer (due to fixed ratio, $a/c = 0.24$) surface crack results in a smaller limit load N^∞ and an earlier penetration, while increased ductility brings counter-results.

Figure 3(a) shows the evolution of CTOA at three different locations with respect to the far field normalized displacement δ_n. At the mid-section ($x/c = 0$), CTOA increases monotonically as δ_n increases, while CTOA near the free surface ($x/c = 0.87$) first drops then increases. Near the end of crack penetration, all CTOA values converge to a constant value CTOA $\simeq 30°$. This results from the drift of the loads applied to each line-spring towards the pure extension mode, with continued crack growth [Fig. 2(b)]. Let the parameter μ measures the local bending-to-tension ratio as $\mu \equiv (M + Na/2)/(Nl)$, where $a(x)$ is the local crack length and $l(x)$ is local remaining ligament. In case of pure extension as represented by $\mu = 0$ of Fig. 5 in Part I, the selected values $A = 0.5$ and $B = 0$ correspond to CTOA $\simeq 30°$ for nonhardening ($n = \infty$) material. We found that at deformation levels $\delta_n \geqslant 3.6$, the average flow stresses τ_o, in all the line-spring finite elements except the one at the free surface, already reached the non-hardening limit value $\tau_o = \tau_u \doteq 1.35\tau_y$. Figure 3(b) is the predicted distribution of CTOA(x) along the crack front at various deformation

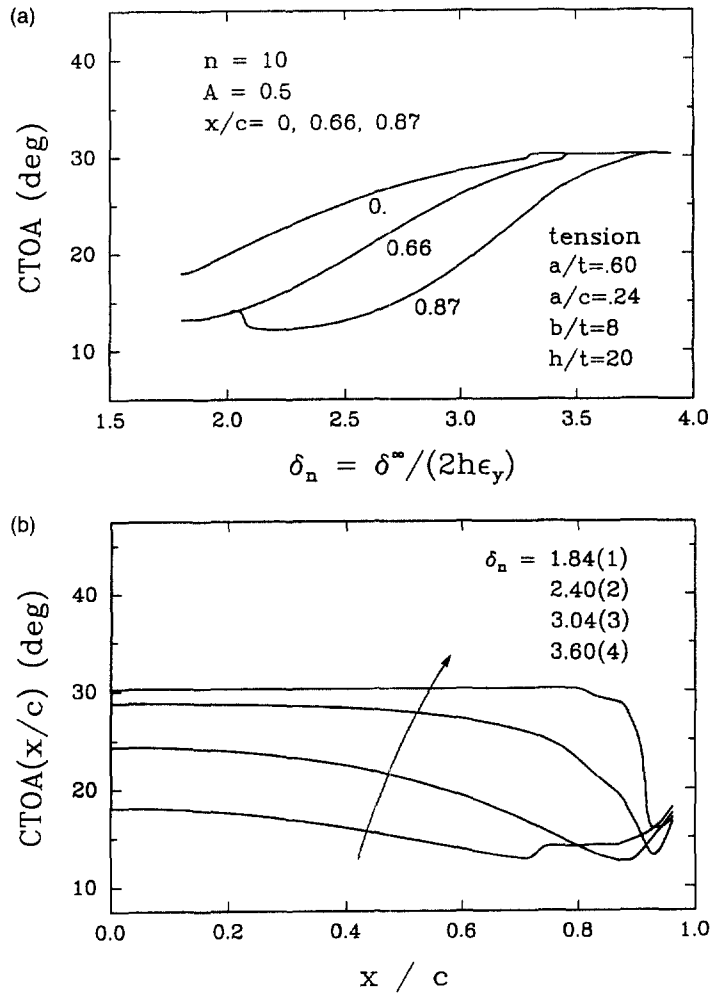

Fig. 3. (a) Variation of CTOA at three different locations with respect to the far field normalized displacement δ_n. (b) Predicted distributions of CTOA (x) along the crack front at various deformation levels.

levels. At the beginning of crack growth, as denoted by $\delta_n = 1.84$, the peak value of CTOA occurs near the intersection with the free surface. As load increases to $\delta_n = 2.4$, CTOA increases in the central part but decreases near the intersection, resulting in a parabola-shaped variation. For the shallow-cracked region near the intersection, we simply used the method for approximate evaluation of CTOA, which strictly applies only for the single slip-line feature of deep cracks. However, all cracks loaded with pure extension mode can be treated as deep cracks irrespective of relative crack depth, because there is no shoulder plastic deformation. On the other hand, cracks having relative crack depth less than about 0.35 mm subject to predominant bending bear quite complicated deformation pattern at the crack-tip (Lee and Parks, 1993). No complete analytical solution for crack-tip stress triaxiality of shallow cracks is currently available. For load levels greater than $\delta_n = 3.6$, at which point the surface crack has almost penetrated the plate thickness—Fig. 4(b), the CTOA along most of the crack front reaches the saturated value of about 30°. The minimum CTOA always occurs near the location $x/c \approx 0.9$, which was also observed in the experiment of RL.

Figure 4(a) represents the penetration of the crack at three locations $x/c = 0$, 0.66 and 0.87. Although same critical value of δ_i^c was used along the surface crack front, cracking at different locations initiates at different far field load levels. If triaxiality dependence of δ_i^c (x/t) were also considered, the crack initiation at $x/c = 0.87$ would be further delayed, because of lower crack-tip constraint at $x/c = 0.87$, as discussed by Wang and Parks (1992).

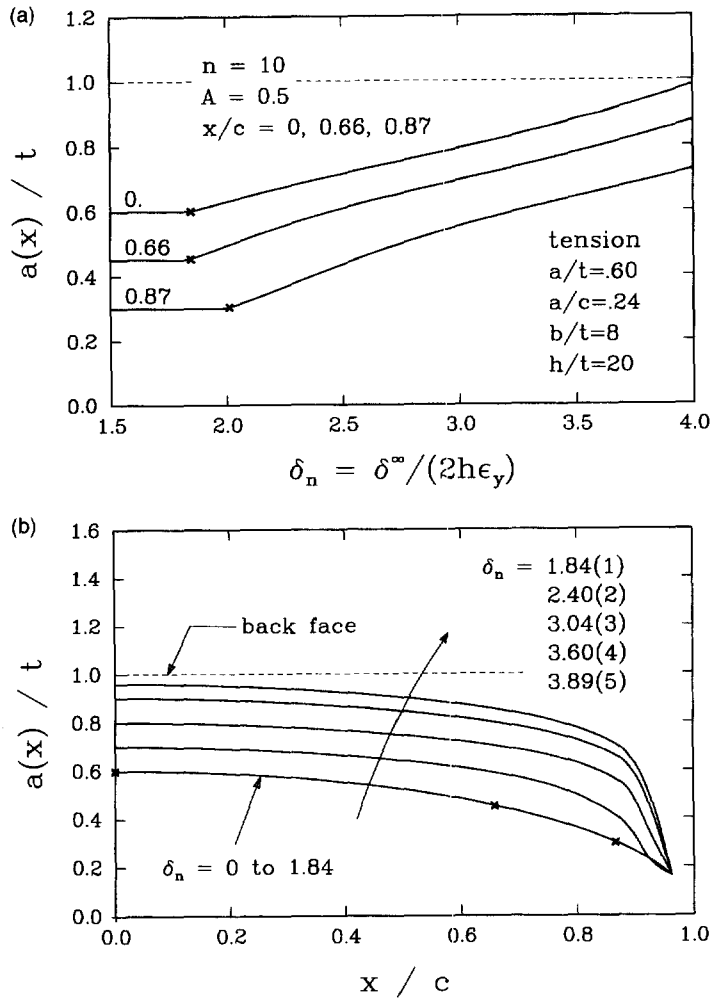

Fig. 4. (a) Evolution of crack depth at the locations $x/c = 0$, 0.66 and 0.87. Although same critical value of δ_t^c was used along the surface crack front, crack initiation at different locations occurs at different far field load levels. (b) Predicted crack front profiles at various deformation levels. The crack remains stationary until $\delta_n \approx 1.84$, whereupon it starts to grow near mid-section.

At the higher load level $\delta_n \geqslant 3.2$, the crack length evolution curves are parallel to each other. This comes from the load state and CTOA variation along the surface crack front. That is, regardless of crack front location, the load state approaches that of pure extension as noted, and consequently CTOA saturates to a constant value. In such case, crack length increment is simply proportional to the far field displacement. Figure 4(b) is the predicted crack front shape at each deformation level. The crack remains stationary until $\delta_n \approx 1.84$, whereupon it starts to grow near mid-section.

As another representative of surface-cracked plate problems in remote extension, we chose a deep and short ($a/t = 0.7$, $a/c = 0.7$) crack in the same-sized plate ($h/t = 20$, $b/t = 16$). Comparison of Fig. 2(a) and Fig. 5(a) reveals that the normalized far-field elongation at the penetration of plate, δ_n^p, strongly depends on the surface crack geometry as well as material hardening. For hardening material ($n = 10$), $\delta_n^p \approx 8.5$ of the short surface crack ($a/c = 0.7$) is more than twice the value of $\delta_n^p \approx 3.85$ of the long surface crack ($a/c = 0.24$). However, each surface crack has almost same value of $\delta_n^p \approx 3$ for $n = \infty$. Trajectories of force and moment transmitted by line-spring elements at three locations during loading, and predicted evolution of CTOA and crack propagation, are presented in Figs 5(b), 6 and 7, respectively, for the deep and short surface crack in the hardening plate. It is worth noting in Fig. 7(b) that along the crack front, surface crack growth relative to its mid-section ($x = 0$) growth is faster in hardening case than in nonhardening case. Unlike

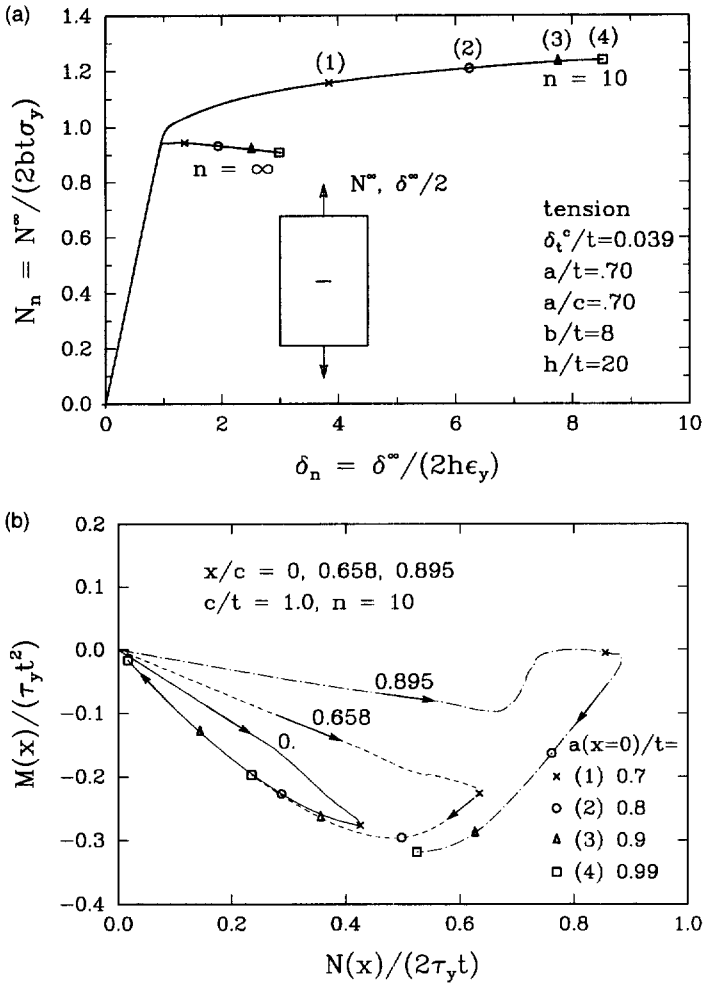

Fig. 5. (a) Normalized load F_n vs displacement δ_n curve for a deep ($a/t = 0.7$), short ($a/c = 0.7$) crack in the same-sized plate ($h/t = 20$, $b/t = 16$) under remote extension. (b) Normalized force and bending moment trajectory transmitted across the line-spring elements at three crack front positions, $x/c = 0$, 0.658 and 0.895.

the long surface crack, lateral extension of this deep and short crack is in fact very likely to happen, since maximum K_I of a semi-circular surface crack occurs on the free surface. However, as the current line-spring model does not account for crack singularities at the free surface, no measure was taken in the analyses to accommodate lateral extension.

3.2. *A pressurized cylindrical vessel with axial surface crack*

In this section, we solve a set of axial surface crack problems in an internally pressurized cylinder having mean radius R_m, a total length $2L$ and a thickness t. The cylinder dimension was fixed at $R_m/t = 10.5$ and $2L/R_m = 11$. As for the surface cracked plate in tension, two-types of semi-elliptical crack configurations, i.e. aspect ratios of ($a/t = 0.6$, $a/c = 0.24$) and ($a/t = 0.7$, $a/c = 0.7$), were selected. Both internal and external crack cases were considered for each crack configuration. No pressure traction, however, was applied to the faces of inner cracks. To form a remotely-closed cylindrical vessel, axial stresses consistent with internal pressure were imposed simultaneously. Figure 8 shows a finite element mesh for $a/t = 0.6$, $a/c = 0.24$ case. It consists of 325 eight-node shell elements and ten line-spring elements arranged to act as the surface crack. Only one-quarter of the cylinder was modeled, again by virtue of symmetries. To facilitate the generation, the mesh was more refined than needed. However, this did not cause any substantial difficulty in computations performed on HP 9000 workstations. A mesh somewhat finer than that in Fig. 8 was employed for the

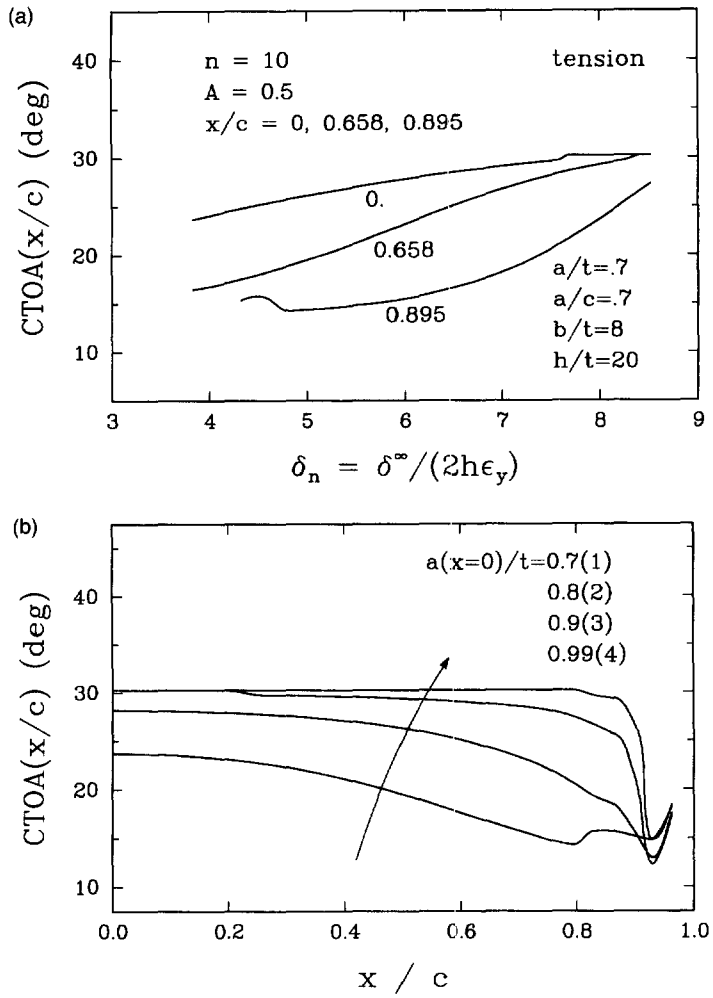

Fig. 6. (a) Variation of CTOA at three different locations with respect to the far field normalized displacement δ_n for the surface crack having $a/t = 0.7$, $a/c = 0.7$. (b) Predicted distributions of CTOA (x/c) along the crack front at various deformation levels.

$a/t = 0.7$, $a/c = 0.7$ case to better define the rapidly varying local crack depth. The same finite element mesh is used for both internal and external crack analyses except that the signs of rotation and moment are reversed in line-spring elements.

Before we probe fully plastic growth, it is instructive to see first some features of stationary cracks in an internally pressurized elastic cylinder. Figure 9(a) and (b) show such elastic stationary crack line-spring solutions of the stress intensity factor K_I and T-stress along the crack fronts. Here average hoop stress $\sigma_h = pR_m/t$ is used for normalizations of K_I and T, and points on the crack front are located by the normalized distance, x/c; see Fig. 1. Poisson's ratio was taken as $\nu = 0.3$. For all four cracks considered, the maximum K_I occurred at the deepest point ($x = 0$). For a given configuration, the external crack carries higher K_I-values than the internal crack. The difference, which comes from less constraint on the rotation at the shell outside, is bigger in the long surface crack. All of these observations parallel the 3-D FEM results by Raju and Newman (1982).

The T-stress is the second term in the Williams (1957) eigen-expansion of elastic crack-tip fields. A pioneering study of Betegón and Hancock (1991) demonstrated that the T-stress quantifies the elastic-plastic crack-tip stress triaxiality; thus, together, the J and T parameters can characterize the elastic-plastic crack-tip fields. For an easier application of two-parameter methodology to surface crack problems, Wang and Parks (1992), and Lee and Parks (1995) extended the line-spring concept to the evaluation of T-stress along the surface crack front. The T-distributions in Fig. 9(b) were obtained following Lee and Parks

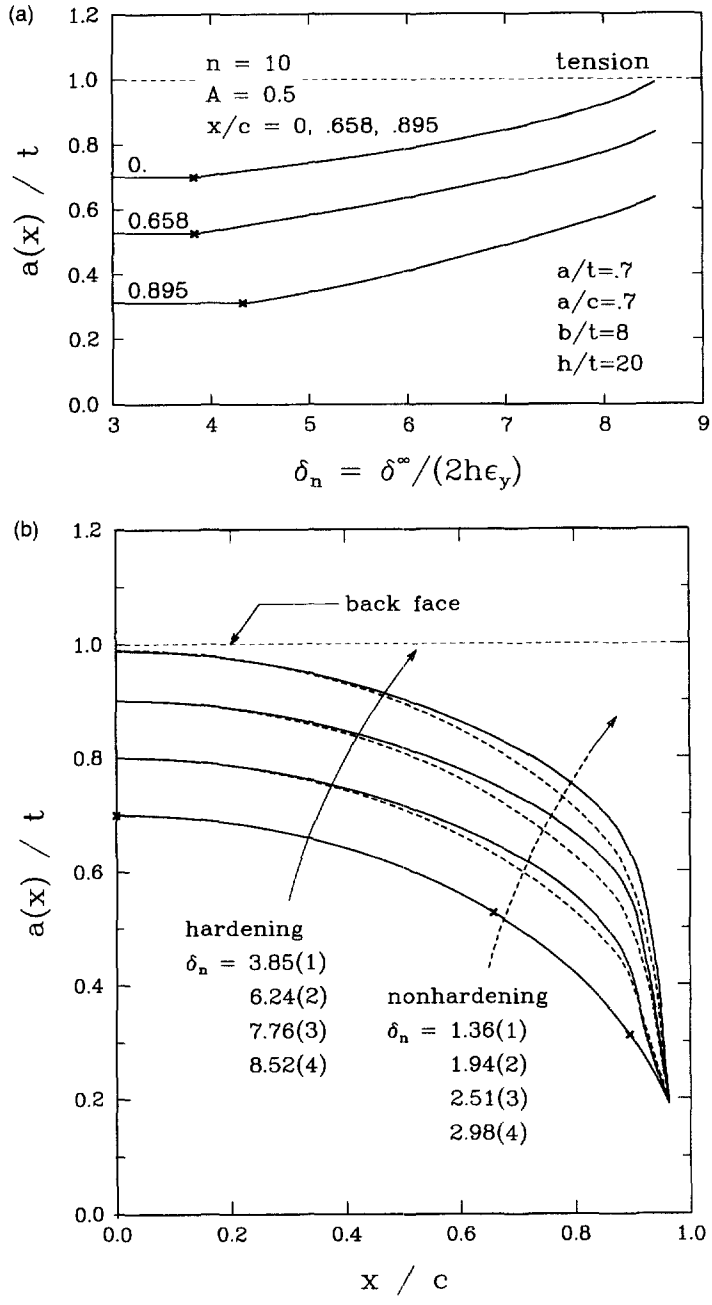

Fig. 7. (a) Evolution of crack depth at the locations $x/c = 0$, 0.658 and 0.895, for the surface crack having $a/t = 0.7$, $a/c = 0.7$. (b) Predicted crack front profiles at various deformation levels. The crack remains stationary until $\delta_n \approx 3.85$, whereupon it starts to grow near mid-section.

(1995). Unlike the plate under remote extension (Wang and Parks, 1992), the pressurized shell here gives continuously varying T-distributions along the crack front for ($a/t = 0.6$, $a/c = 0.24$) crack geometry. Overall, negative T-stress can be related to the enhanced resistance to tearing, and increased CTOA whereby allowing stable crack growth (Hancock *et al.*, 1993).

For the long surface crack ($a/t = 0.6$, $a/c = 0.24$), Fig. 10(a) shows the local crack penetrations at three locations, $x/c = 0.$, 0.66 and 0.87 with respect to the normalized internal pressure, $p_n = pR_c/(\sigma_y t)$. Material properties were taken such that $\sigma_y/E = 0.0023$, $n \doteq 10$; $A = 0.5$, $B(\sigma_y) = 0$ and $\delta_t^c/t = 0.15$ mm/6.4 mm $\doteq 0.024$. Local crack initiations, marked by the '$\times$' symbols, occur consistently earlier in the external crack than in the

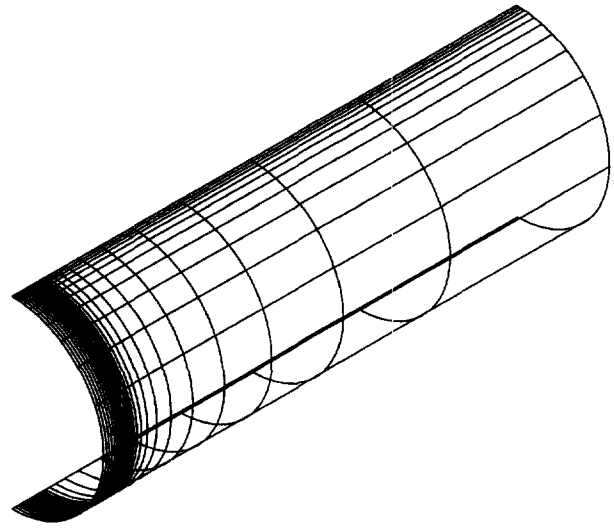

Fig. 8. A finite element mesh for axial surface cracks of $a/t = 0.6$, $a/c = 0.24$ configuration in an internally pressurized cylinder.

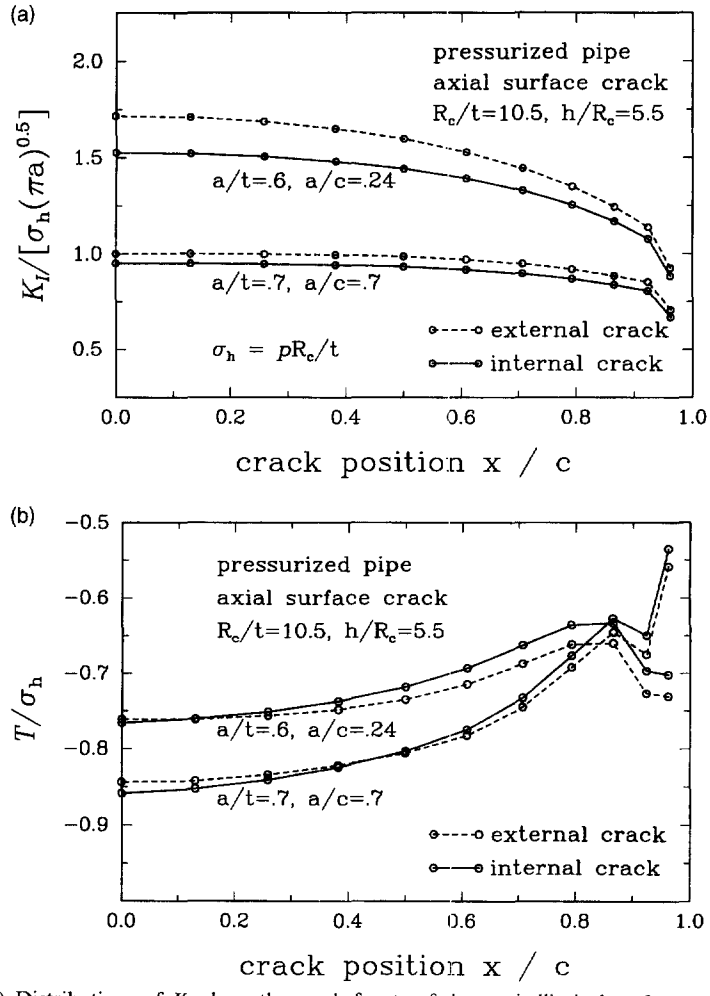

Fig. 9. (a) Distributions of K_I along the crack fronts of the semi-elliptical surface cracks in an internally pressurized vessel. (b) Distributions of T-stress along the crack fronts of the semi-elliptical surface cracks in an internally pressurized vessel.

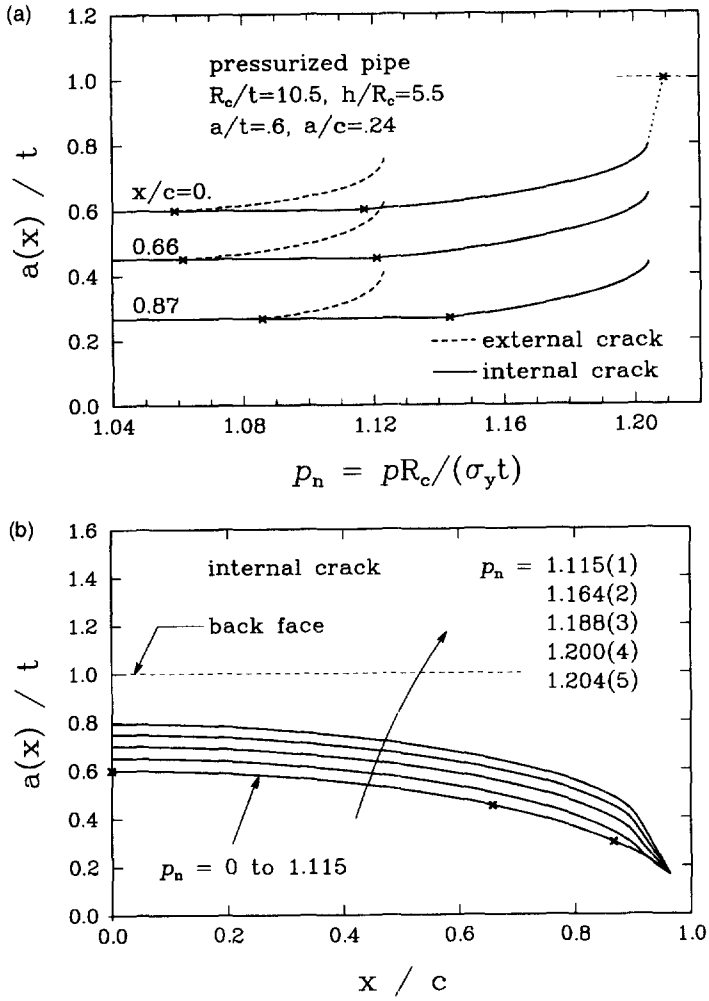

Fig. 10. (a) Local crack propagations at three locations, $x/c = 0$, 0.66 and 0.87 with respect to the normalized internal pressure, $p_n = pR_m/(\sigma_y t)$ for the long surface crack. (b) Enlargement of the internal crack surface with increasing applied internal pressure.

internal crack, as expected from Fig. 9(a). In contrast to the plate under displacement-controlled remote extension of Fig. 4(a), here the crack growth is sharply accelerated with increasing applied internal pressure. Computations were in fact carried out only near to points of maximum pressure due to numerical convergence problems. Linear extrapolation of the last two increments can provide estimates of the normalized penetration pressure; $p_n = 1.13/1.21$ for external/internal cracks, respectively. The issue involved in the fully plastic solution from the 'pressurized' shell finite element model is addressed in the discussion section. Figure 10(b) shows the gradual enlargement of the internal crack surface as the applied internal pressure increases. Note that over each (evenly-spaced) enlargement, pressure increment drops by one-half. Local CTOA evolution vs p_n at three locations along the internal surface crack front are plotted in Fig. 11(a). Near, $p_n = 1.205$, the CTOAs sharply increase to CTOA $\simeq 31.4°$, a maximum for model parameter $n \doteq 10$ and $A = 0.5$. Variations of CTOA along the crack front at differing internal pressure levels are given in Fig. 11(b). The reversal of distribution shape between CTOA and T-stress of Fig. 9(b) is a natural outcome of quantifying crack-front fields based on both deformation and stress. Peak values of CTOA always occur at the center line ($x = 0$) through the loading.

Figure 12(a) depicts the local crack extension vs normalized internal pressure at $x/t = 0.$, 0.658 and 0.895 of the deep and short crack ($a/t = 0.7$, $a/c = 0.7$). A slightly earlier initiation in the external than internal crack is again consistent with the K_I-distribution of

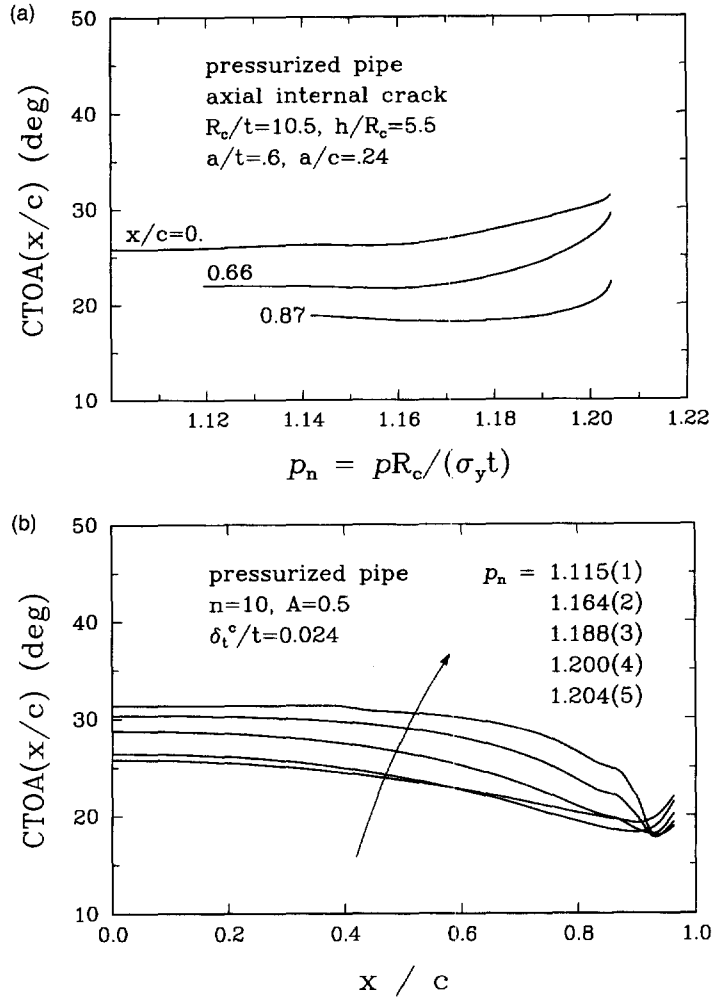

Fig. 11. (a) Local CTOA evolution vs p_n at three locations along the internal surface crack front. (b) Variations of CTOA along the crack front at differing internal press levels.

Fig. 9(a). Acceleration of crack extension with increasing p_n is gradual here, and no numerical convergence problem occurred (until the center-line penetration). Comparison of the enlargement patterns of internal and external cracks in Fig. 12(b) reveals that the local crack growth relative to the center-line crack extension is faster in the external crack. The same feature was observed in the foregoing long crack, although not shown. Local CTOA evolution vs p_n at three locations, and CTOA variations at differing relative center-line crack depth, $a(x = 0)/t$, are plotted in Fig. 13(a) and (b), respectively. At the moment of center-line penetration, $a(x = 0)/t = 0.98$, CTOA has reached its maximum value along nearly the entire crack front. Again, no special measure was taken into the present analyses for a possible lateral extension in the deep and short crack.

3.3. *A pipe bending problem*

Our line-spring model now targets a circumferentially-cracked pipe subject to pure bending load. Figure 14 shows schematics of the pipe with an internal surface crack, and a corresponding finite element shell model used for both internal and external cracks. Twelve line-spring elements were placed to represent the cracked plane. A long and constant relative crack depth geometry was taken such that $a(\gamma)/t = 0.66$ and $\gamma_o = 93.6^\circ$ in Fig. 14(a). Here γ measures angular distance along the crack front from the center-line over an arc of total extent $2\gamma_o$, where $\gamma_o = 93.6^\circ$. It is on this crack geometry and loading that Kikuchi (1992) reported a remarkably relaxed plane strain crack-tip stress field, approaching that of a

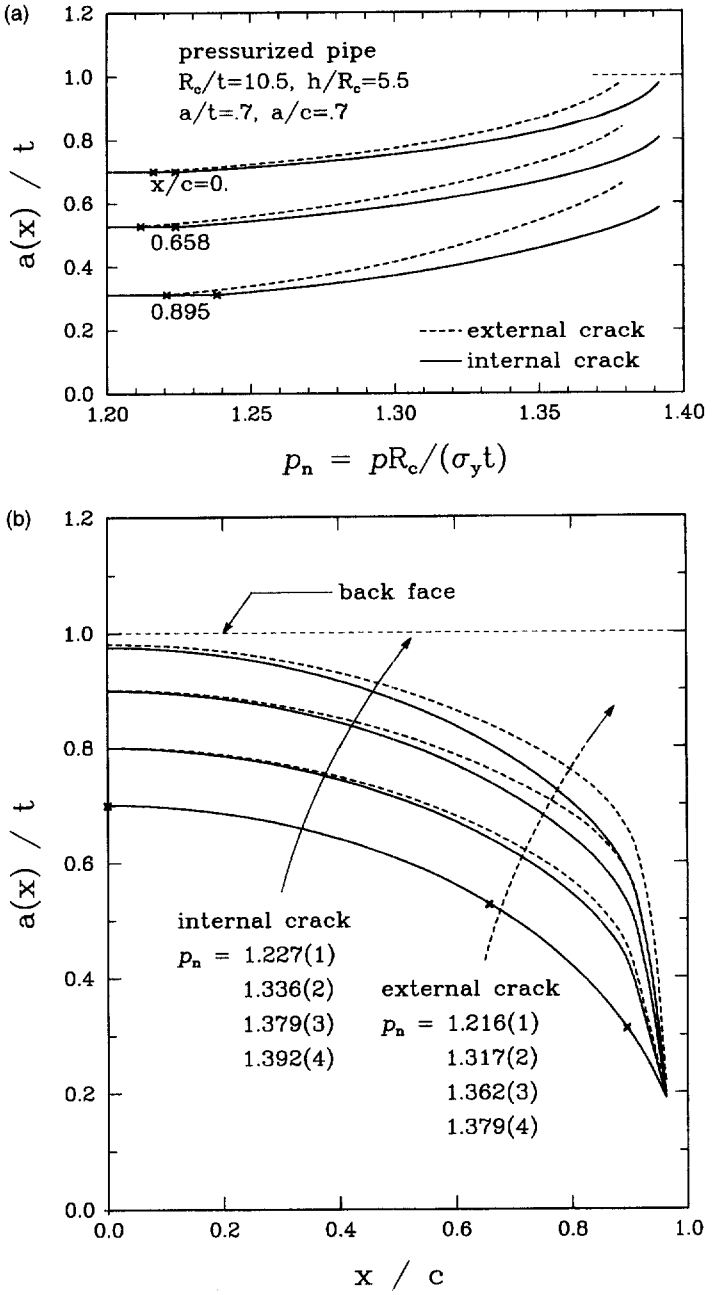

Fig. 12. (a) Local crack extension vs normalized internal pressure at $x/c = 0$, 0.658 and 0.895 of the deep and short crack ($a/t = 0.7$, $a/c = 0.7$). (b) Comparison of the enlargement patterns of internal and external cracks of the deep and short crack ($a/t = 0.7$, $a/c = 0.7$).

plane stress crack-tip. Figures 15(a) and (b) show the crack-front distributions of the elastic stress intensity factor K_I and T-stress, normalized with the tensile stress of the outer-fiber in the uncracked-pipe cross section, $\sigma_b = M^\infty(R_c + t/2)/I$, where I is the second moment of the uncracked-pipe cross sectional area. These preliminary elastic solutions clarify the fact that crack-tip fields near center-line ($\gamma/\gamma_o = 0$) experience intense deformation very low constraint (very negative T-stress), while those near the crack end ($\gamma/\gamma_o = 1$) undergo small deformation under relatively low constraint. We therefore expect that the local crack fronts near center-line will propagate in a stable manner without any sensible lateral extension. It is also worth noting that $T/\sigma_b \approx -0.9$ at the center-line is the most negative T-value for nominal tension ever known, except that of the Griffith crack ($T/\sigma^\infty = -1$). Figure 16(a)

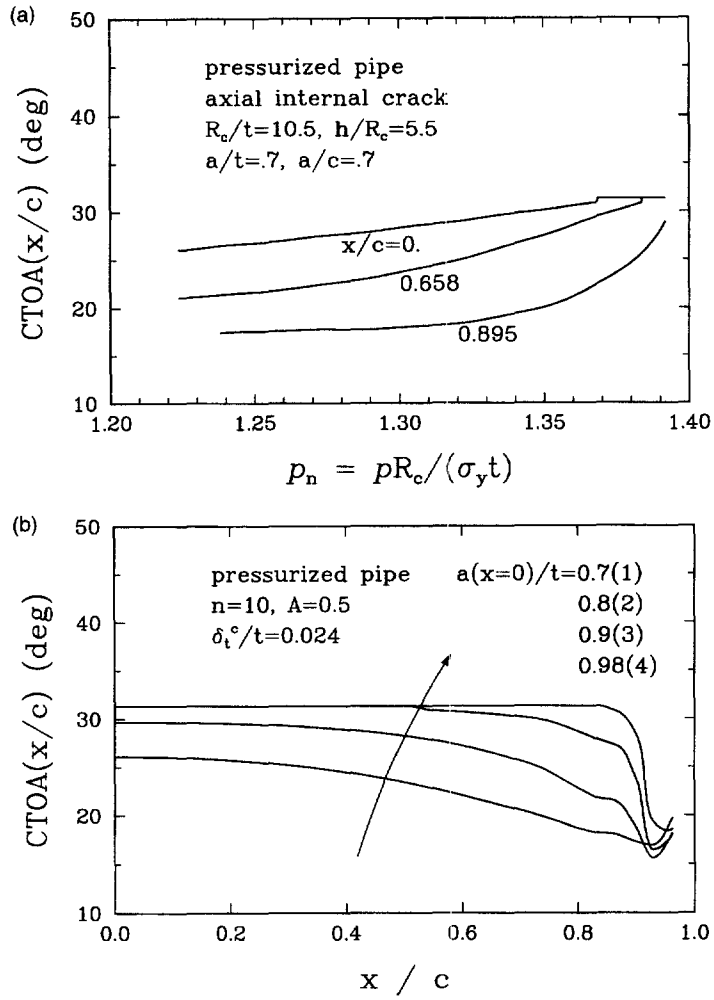

Fig. 13. (a) Local CTOA evolution vs p_n at three locations. (b) CTOA variations at differing relative center-line crack depth $a(x = 0)/t$.

is the normalized moment vs rotation curve, where ϕ_y and M_y are the rotation and moment, respectively, at incipient yielding of outer-fiber in the uncracked-pipe cross section. Following Kikuchi (1992), material properties were taken such that $\sigma_y/E = 0.001$, $n \doteq 4$; $A = 0.5$, $B(\sigma_s) = 0$ and $\delta_t^c/t = 0.15$ mm/16.6 mm $\doteq 0.01$. The reaction moments drop significantly near penetration due to the substantial amount of net-section reduction far from the neutral axis. The external crack grows faster than the internal one again. Figure 16(b) shows the enlargement pattern of the external crack surface as the applied rotation increases. The crack grows much faster near center-line than near free surface, as expected from Fig. 15. Local CTOA evolution and crack propagation at the external crack front locations $\gamma/\gamma_o = 0$, 0.5 and 0.792 are given in Figs 17(a) and (b), respectively. CTOA is observed to saturate to CTOA $\simeq 32.9°$, a maximum for given $n \doteq 4$ and $A = 0.5$.

4. DISCUSSION

RL (Reuter and Lloyd, 1990) interpreted their experimental CTOA vs Δa result (Fig. 17 of RL) as indicating the trend of decreasing CTOA with increasing crack depth as applied load increases. The fatigue precracked specimen initially undergoes blunting, then passing through the transient stages, it reaches quasi-steady state growth. In the experiments of RL, the initially large value of CTOA seems essentially due to the blunting ($\Delta a < 0.2$ mm), and no data are shown for 0.2 mm $< \Delta a <$ 1 mm. Further, the tested replicate

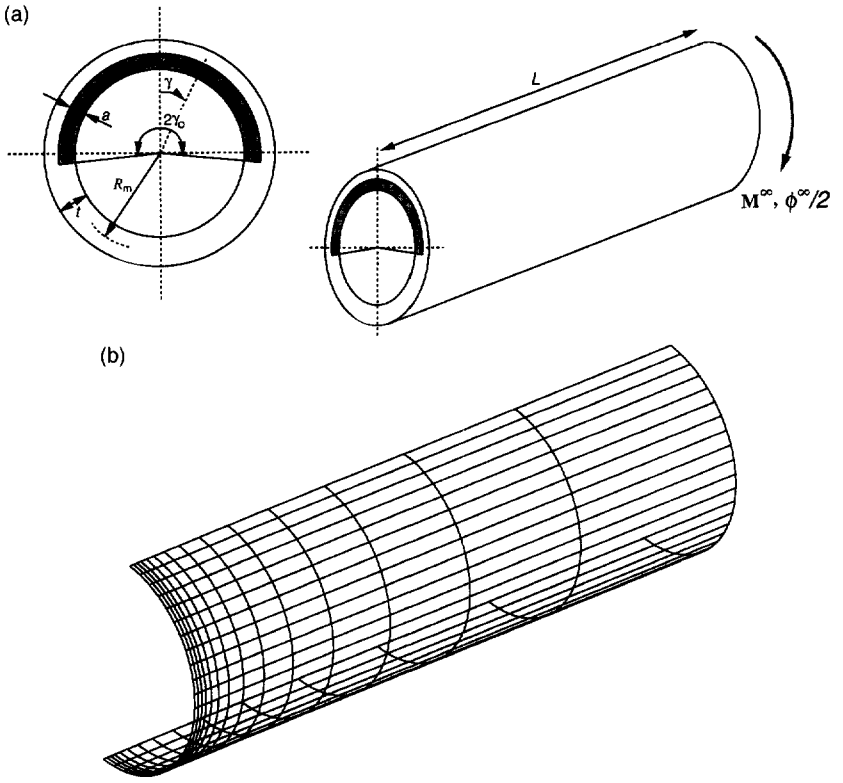

Fig. 14. (a) Schematics of the pipe with an internal circumferential surface crack, subject pure bending. (b) A corresponding finite element shell model used for both internal and external cracks.

specimens contain about 10% variation in their maximum center-line crack depth of fatigued pre-cracks. For these and other reasons such as large compliancies from the testing machine, extensions, adapters and grips, direct quantitative comparison between experimental results and the line-spring simulation is rather difficult. Our fully plastic line-spring model, which takes only steady state growth into consideration, shows a gradual increase of CTOA at the center-line immediately after the crack initiation. Combining experimental and FEM results, we infer that the CTOA at center-line of the surface crack under remote extension drops to a lower value after blunting, then it gradually increases and finally saturates to a constant value. Experiments of RL also show a tendency for CTOA to approach a constant value of about 40° with increasing crack depth. As remarked, the load state along the crack front of surface crack under remote extension approaches the pure extension mode ($N > 0$, $M < 0$; $\mu \approx 0$). Reverse-calculating of A with $\mu = 0$, $B = 0$ and CTOA = 30° ~ 40° from (1)–(3) of Part I gives $A = 0.5 \sim 0.6$. On this basis, we adopted $A = 0.5$ and $B = 0$ for the surface crack analyses. McClintock *et al.* (1995b) suggested some plane strain, fully plastic growth tests for determining the material properties A and $B(\sigma_s)$ from unequally grooved tensile specimens.

For circumferentially cracked Type-304 stainless steel pipes in fully plastic tension, Zahoor and Norris (1984) demonstrated that a strong propensity for predominantly radial growth exists. They also showed that pipes of similar size but reduced thickness are expected to show greater potential for leak-before-break (LBB). For the part-through circumferential crack in pipes subject to bending, Zahoor and Kanninen (1981) predicted that crack growth in the circumferential direction prior to the wall break-through will be negligible. Experimental observations on surface cracked plates under remote extension (RL) and remote bending (White *et al.*, 1983) indeed showed negligible crack growth in the lateral direction. However, as inferred from the K_I-distribution along a deep semi-circular surface crack front (Raju and Newman, 1979), where the maximum K_I occurs at the free surface, the deep and short crack is very likely to first extend in the lateral direction. Provided an

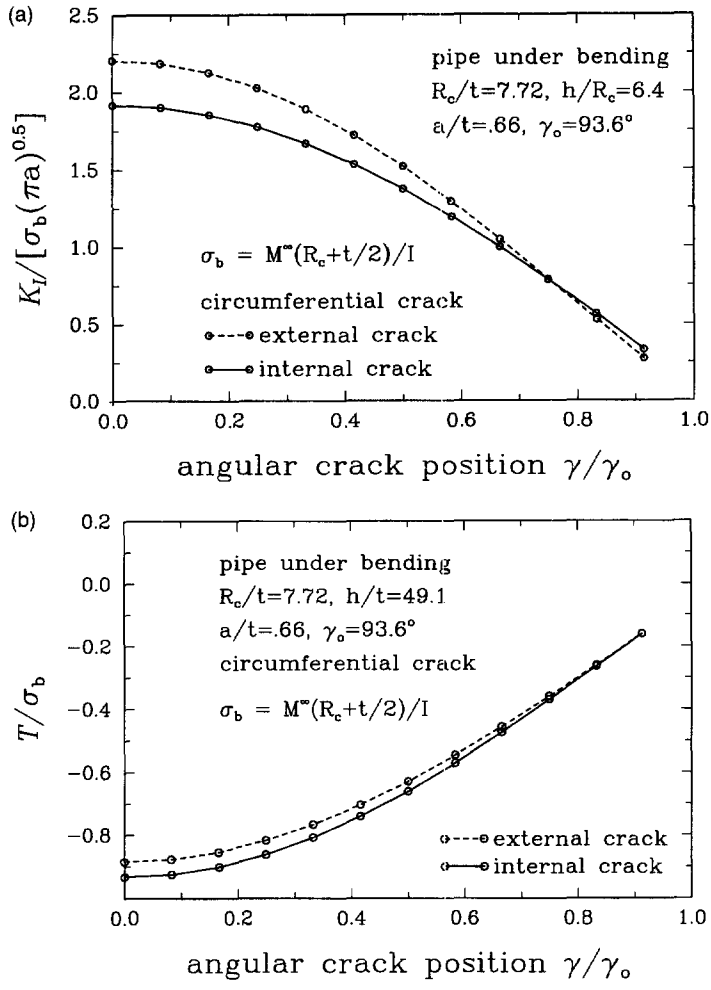

Fig. 15. (a) Distributions of K_I along the crack fronts of the long circumferential surface cracks in a pipe subject to bending. (b) Distributions of T-stress along the crack fronts of the long circumferential surface cracks in a pipe subject to bending.

appropriate criterion can be incorporated, in the line-spring model, the lateral extension of a surface crack can be accommodated by adding a few line-spring finite elements with initially zero crack depth just adjacent to free surface intersection.

Kumar and German (1985) showed that the thin-shell finite element method does not accurately handle the problem of an internally pressurized cylinder under fully plastic condition. The solution error (in deformation as a function of pressure) increases with increasing strain hardening exponent, n and decreasing ratio of mean radius to thickness, R_c/t. To overcome this difficulty, they suggested that the fully-plastic cracked-cylinder should be modeled by 3-D brick elements rather than shell elements. Therefore, for more quantitatively precise fully plastic solutions, our line-spring elements could be also connected to the 3-D brick elements by using multi-point constraints (MPC) option in ABAQUS (1993b).

When a cracked pipe with an internal part-through circumferential crack is subject to pure bending as in Fig. 14(a), the load states along the crack front are located at the vertex of the yield surface, corresponding to local mid-ligament tension. In contrast to pure extension, this loading states cause the yield surface normal to have negative plastic rotation component. Although we know the two extreme values of the yield surface normals at the vertex, for simplification of the numerical procedure, we preferentially used the smooth continuation of the yield surface at the vertex in ABAQUS finite element code (1993a); improved models of this phenomenon should be further investigated.

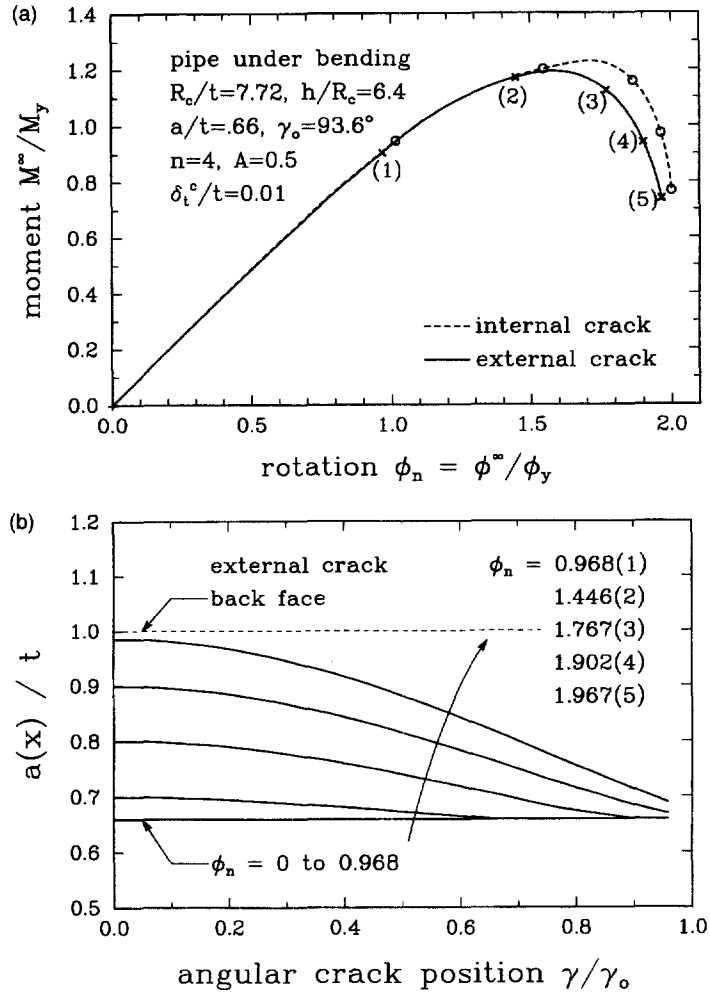

Fig. 16. (a) Normalized reaction moment vs applied rotation curves for a circumferentially cracked pipe subject to bending. (b) Enlargement pattern of the external crack surface with increasing applied rotation.

As noted in Part I, our line-spring model formulated on small-geometry change does not account for bulging or wall-thinning behavior. However, unlike the through-crack in a 2-D SEC specimen, finite length surface cracks embedded in plates/shells are less exposed to bulging due to the geometrical resistance from their elastic surroundings. Accordingly, the bulging effect is less important in surface crack problems presented here. However, the pipe ovalization on bending, the Brazier effect, does require large geometry analysis, as does the effects of changing R_c/t with plastic deformation under internal pressure. These effects are under investigation in the present model.

Significant anisotropy can occur in nuclear pipes due to forming or manufacturing process. Wilkowski (1991) reported that the anisotropy of material can cause the crack under initially pure mode I loading to turn and grow with mode II or mode III components. The change in failure mode may bring error into the assessment of postulated cracks under mode I loading. Thus LBB analyses for combined modes may be necessary.

5. SUMMARY

The line-spring model based on the CTOA crack growth criterion was applied to the crack-growth problems of surface cracks in plate/pipe structures under fully plastic conditions. In the line-spring model, the CTOA is evaluated using the sliding-off and shear-cracking model together with the least upper bound method. The constraint-dependent

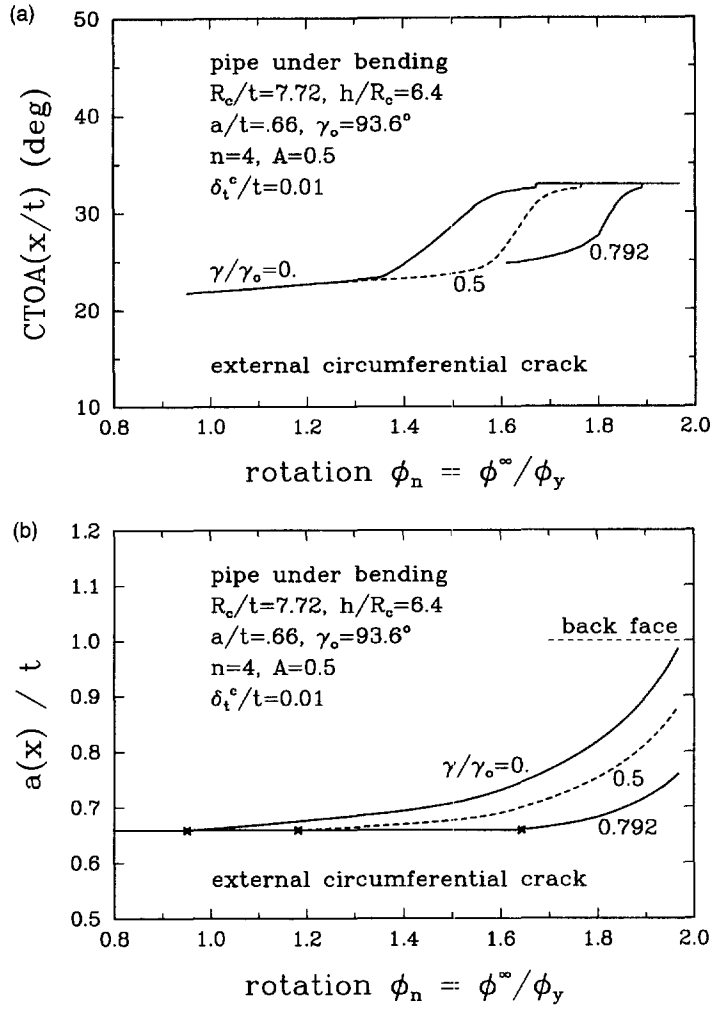

Fig. 17. (a) Local CTOA evolution at the external crack front locations γ/γ_o = 0, 0.5 and 0.792. (b) Local crack propagation at the external crack front locations γ/γ_o = 0, 0.5 and 0.792.

CTOA, which varies both along the surface crack and with respect to the applied load (Figs 6, 11, 13 and 17(b)), determines the increment of crack extension from the kinematic relation with the CTOD increment.

Simulation of ductile surface crack growth in a plate under remote extension showed that the remote reaction force of a long surface-cracked plate with hardening material saturates after fully plastic yielding, while that with non-hardening material steadily decreases. The ligament-load states along the surface crack front eventually approach pure extension. Combination of the experimental results of Reuter and Lloyd (1990) and our line-spring simulation suggests that the center-line CTOA drops to a lower value after blunting, then it gradually increases and finally saturates to a constant value. For hardening material, the normalized far-field elongation at plate penetration, δ_n^p, of the short surface crack is more than twice the value for δ_n^p of the long surface crack, while the lower δ_n^p of each surface crack is almost the same for nonhardening material.

When a cylinder with an axial surface crack is internally pressurized, the crack initiates earlier and propagates faster in external as compared to internal cracks. In contrast to the plate under displacement-controlled remote extension, the crack growth in an internally pressurized cylinder is sharply accelerated with increasing applied internal pressure. The local crack growth relative to the center-line crack extension is faster in the external crack. For a circumferentially cracked pipe subject to pure bending load, $T/\sigma_b \approx -0.9$ was obtained at the center-line, the most negative one ever since the Griffith crack. Near

through-thickness penetration, a sharp and significant reaction moment drop results from the substantial amount of net-section reduction, and the external crack grows faster than the internal one again.

Acknowledgments—This work was supported by the Office of Basic Energy Sciences, Department of Energy, under Grant No. DE-FG02-85ER13331. Computations were performed on HP 9000 workstations obtained under NSF Grant No. DDM-8914161. The ABAQUS finite element program was made available under academic license from Hibbitt, Karlsson and Sorensen Inc., Pawtucket, RI. Useful interactions with Dr. W. G. Reuter and Mr. W. R. Lloyd of the Idaho National Engineering Lab. are also acknowledged.

REFERENCES

ABAQUS Theory Manual (1993a) Version 5.3, Hibbitt, Karlsson and Sorensen, Inc., Pawtucket, RI.

ABAQUS User's Manual (1993b) Version 5.3, Hibbitt, Karlsson and Sorensen, Inc., Pawtucket, RI.

Betegón, C. and Hancock, J. W. (1991) Two-parameter characterization of elastic-plastic crack tip fields. *Journal of Applied Mechanics* **58,** 104–110.

Hancock, J. W., Reuter, W. G. and Parks, D. M. (1993) Constraint and toughness parameterized by *T*. In *Constraint Effects in Fracture*, ASTM STP 1171, ed. E. M. Hackett *et al.*, pp. 21–40.

Hutchinson, J. W. and Paris, P. C. (1979) Stability analysis of *J*-controlled crack growth. In *Elastic-Plastic Fracture*, ASTM STP 668, ed. J. D. Landes *et al.*, pp. 37–64.

Kanninen, M. F. and Popelar, C. H. (1985) *Advanced Fracture Mechanics*, Chapter 1. Oxford University Press, New York.

Kikuchi, M. (1992) Analysis of HRR fields of surface cracks. *International Journal of Fracture* **58,** 273–283.

Kim, Y.-J., McClintock, F. A. and Parks, D. M. (1996) Global equilibrium of the least upper bound circular arcs and its application to fracture mechanics. Accepted for publication, *International Journal of Fracture*.

Kumar, V. and German, M. D. (1985) Studies of the line-spring model for nonlinear crack problems. *Journal of Pressure Vessel Technology* **107,** 412–420.

Lee, H. and Parks, D. M. (1993) Fully plastic analyses of plane strain single-edge cracked specimens subject to combined tension and bending. *International Journal of Fracture* **63,** 329–349.

Lee, H. and Parks, D. M. (1995) Enhanced elastic-plastic line-spring finite element. *International Journal of Solids and Structures* **32,** 2393–2418.

Lee, H. and Parks, D. M. (1998) Line-spring finite element for fully plastic crack growth—I. Formulation & one-dimensional results. *International Journal of Solids and Structures* **35,** 5115–5138.

McClintock, F. A., Kim, Y.-J. and Parks, D. M. (1995) Tests for fully plastic fracture mechanics of plane strain mode I crack growth. In *Constraint Effects in Fracture: Theory and Applications*, ASTM STP 1256, ed. M. Kirk and A. Bakker, pp. 199–222.

Miyoshi, T., Shiratori, M. and Yoshida, Y. (1986) Analysis of *J*-integral and crack growth for surface cracks by line-spring method. *Journal of Pressure Vessel Technology* **108,** 305–311.

Parks, D. M. (1981) The inelastic line-spring: estimates of elastic-plastic fracture mechanics parameters for surface-cracked plates and shells. *Journal of Pressure Vessel Technology* **103,** 246–254.

Parks, D. M. and White, C. S. (1982) Elastic-plastic line-spring finite elements for surface-cracked plates and shells. *Journal of Pressure Vessel Technology* **104,** 287–292.

Raju, I. S. and Newman, J. C., Jr. (1979) Stress intensity factors for a wide range of semi-elliptical surface cracks in finite-thickness plates. *Engineering Fracture Mechanics* **11,** 817–829.

Raju, I. S. and Newman, J. C., Jr. (1982) Stress-intensity factors for internal and external surface cracks in cylindrical vessels. *Journal of Pressure Vessel Technology* **104,** 293–298.

Reuter, W. G. and Lloyd, W. R. (1990) Measurements of CTOD and CTOA around surface-crack perimeters and relationships between elastic and elastic-plastic CTOD values. In *Surface-Crack Growth: Models, Experiments, and Structures*, ASTM STP 1060, ed. W. G. Reuter *et al.*, pp. 152–176.

Rice, J. R. (1972) The line-spring model for surface flaws. In *The Surface Crack: Physical Problems and Computational Solutions*, ed. J. L. Swedlow, pp. 171–185. American Society of Mechanical Engineers, New York.

Rice, J. R. (1975) Elastic-plastic models for stable crack growth. In *Mechanics and Mechanisms of Crack Growth*, Proceedings of Conference at Cambridge, England, ed. M. J. May, pp. 14–39. British Steel Corporation Physical Metallurgy Center Publication.

Rice, J. R. and Levy, N. (1972) The part-through surface crack in an elastic plate. *Journal of Applied Mechanics* **39,** 185–194.

Wang, Y.-Y. (1993) On the two-parameter characterization of elastic-plastic crack-front fields in surface-cracked plates. In *Constraint Effects in Fracture*, ASTM STP 1171, ed. E. M. Hackett, K.-H. Schwalbe and R. H. Dodds Jr., pp. 120–138.

Wang, Y.-Y. and Parks, D. M. (1992) Evaluation of the elastic *T*-stress in surface-cracked plates using the line-spring method. *International Journal of Fracture* **56,** 25–40.

White, C. S., Ritchie, R. O. and Parks, D. M. (1983) Ductile growth of part-through surface cracks: experiment and analysis. In *Elastic-Plastic Fracture: Second Symposium, Volume I—Inelastic Crack Analysis*, ASTM STP 803, ed. C. F. Shih and J. P. Gudas, pp. I-384–I-409.

Wilkowski, G. M. (1991) Anisotropic fracture toughness effects on failure modes of piping. *Journal of Pressure Vessel Technology* **113,** 154–158.

Williams, M. L. (1957) On the stress distribution at the base of a stationary crack. *Journal of Applied Mechanics* **24,** 111–114.

Zahoor, A. and Kanninen, M. F. (1981) A plastic fracture instability analysis of wall breakthrough in a circumferentially cracked pipe subjected to bending loads. *Journal of Engineering Material Technology* **103,** 194–200.

Zahoor, A. and Norris, D. M. (1984) Ductile fracture of circumferentially cracked type-304 stainless steel pipes in tension. *Journal of Pressure Vessel Technology* **106,** 399–404.